Complex dynamics in nanosystems

Xuan Ni, Lei Ying, Ying-Cheng Lai, Younghae Do, and Celso Grebogi

Complex dynamics in nanosystems

Xuan Ni,[1] Lei Ying,[1] Ying-Cheng Lai,[1, 2, 3] Younghae Do,[3] and Celso Grebogi[2]

[1]*School of Electrical, Computer and Energy Engineering,*
Arizona State University, Tempe, Arizona 85287, USA
[2]*Institute for Complex Systems and Mathematical Biology,*
King's College, University of Aberdeen, Aberdeen AB24 3UE, UK
[3]*Department of Mathematics, Kyungpook National University, Daegu, 702-701, South Korea*

Complex dynamics associated with multistability has been studied extensively in the past but mostly for low-dimensional nonlinear dynamical systems. A question of fundamental interest is whether multistability can arise in high-dimensional physical systems. Motivated by the ever increasing widespread use of nanoscale systems, we investigate a prototypical class of nanoelectromechanical systems: electrostatically driven Si-nanowires, mathematically described by a set of driven, nonlinear partial differential equations. We develop a computationally efficient algorithm to solve the equations. Our finding is that multistability and complicated structures of basin of attraction are common types of dynamics, and the latter can be attributed to extensive transient chaos. Implications of these phenomena to device operations are discussed.

I. INTRODUCTION

Multistability and transient chaos are common in nonlinear dynamical systems. Phenomena associated with multistability such as fractal basin boundaries, riddled and intermingled basins, and noise-induced hopping have been extensively studied in the past three decades[1]. However, most previous studies on multistability were focused on relatively low-dimensional dynamical systems[2] that, mathematically, are often described by ordinary differential equations (ODEs). The aim of this paper is to examine multistability in terms of complex dynamics and implications in a class of high-dimensional, physically significant, nanoelectromechanical (NEM) systems at the frontier of interdisciplinary research: electrostatically driven nanowire systems. Such systems are characterized by their small size, extremely low power consumption, and ultra fast speed. Applications range from Zeptogram scale mass sensing[3] and single electron spin detection[4] to RF communication[5], semiconductor superlattice[6,7] and many others[8,9]. We note that multistability in micro-scale systems has been previously uncovered and studied, such as a mixed behavior in nonlinear micromechanical resonators[10] and multistable micro actuator with serially connected bistable elements[11].

A fundamental goal of science is to have an experimentally validated, predictive theory based on a set of physical laws. With such a theory, a question of concern is whether the final state can be predicted from an initial state chosen in the vicinity of a basin boundary, due to the inevitable error in the specification of the initial state. Here, the basin of attraction of an attractor is the set of initial conditions in the phase space that approach asymptotically the attractor, and the basin boundary separates the initial states leading to different final asymptotic states or attractors. In nonlinear dynamical systems, it is common for basin boundaries to be fractal[1]. In this case, the ability to predict the final attractor of the system may be compromised dramatically. Whether multistability can arise in nanosystems and its dynamical consequences on device performance are thus fundamental issues that need

to be investigated for the design and development of nanoscale devices.

There were previous works on nonlinear dynamics in nanosystems, such as synchronized oscillations in coupled nanomechanical oscillators[12], signal amplification and stochastic resonance in silicon-based nanomechanical resonators[13], and extensive chaos in driven nanowire systems[14]. However, to explore multistability and complex basin structures in driven nanowire systems is extremely challenging, because a physically realistic model of such systems is mathematically described by a set of nonlinear partial differential equations (PDEs), and it is necessary to examine solutions from a very large number of initial states. In the traditional framework of finite-element method (FEM)[15], the solution is obtained by solving a matrix equation, where the matrix elements need to be evaluated in an iterative manner, a task that can be computationally extremely demanding especially for physically detailed models. Taking advantage of the specific physics associated with the driven nanowire system, we *find* that, surprisingly, a large set of matrix elements arising from the finite-element paradigm can in fact be evaluated analytically, reducing tremendously the integration time. Our main *finding* is that multistability can occur in wide parameter regime of the driven Si-nanowire system, and the origin of complex basin dynamics can be attributed to high-dimensional transient chaos permeating the phase space. A practical implication is that, because of the intrinsic difficulty to predict the final state of the system, and because of the tendency for the system to occasionally switch from one stable state to another under disturbances, parameter regimes in which multistability and complex basin dynamics arise should be avoided in the design and development of nanowire devices.

Our model of physically detailed, electrostatically driven Si-nanowire system is described in Sec. II. Transient behavior and the dynamical mechanism of multistability are analyzed in Sec. III with the aid of extensive frequency analysis. Basin structures and their characterization are presented in Sec. IV, and the ubiquity of multistability in the driven nanowire sys-
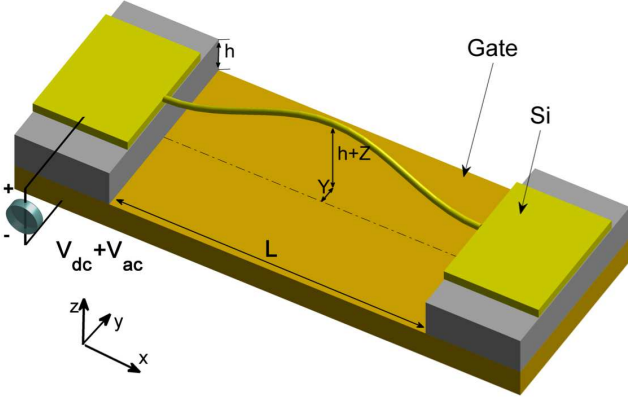
FIG. 1: (Color online) Schematic diagram of a driven nanowire system. A thin, electrostatically driven Si nanowire of length L and diameter d is suspended on a U-shaped gate. The gap between the wire and the gate is h. The oscillations can be non-planar in both y and z directions, even though the driving is along z.

tem is demonstrated in Sec. V. Concluding remarks are offered in Sec. VI, and our efficient numerical procedure for solving the nonlinear PDEs of the driven nanowire system is outlined in Appendix.

II. MODEL OF DRIVEN SI NANOWIRE

Consider a driven nanowire system, as shown schematically in Fig. 1. For a beam with ends clamped and subject to large deformation, the equations of motion are

$$\rho A \partial_t^2 Y + EI \partial_x^4 Y - \frac{EA}{2L} I_0 \partial_x^2 Y = F_f^Y,$$
$$\rho A \partial_t^2 Z + EI \partial_x^4 Z - \frac{EA}{2L} I_0 \partial_x^2 Z = F_f^Z + F_e, \quad (1)$$

where $Y(x,t)$ and $Z(x,t)$ are the displacements in y, z directions, respectively, E is the Young's modulus, ρ is the volume density, L is the original wire length, A is the cross-sectional area, $I = \pi r^4/4$ is the cross-sectional moment of inertia of the wire, and I_0 is an integral proportional to the length increment of the wire under stretch, which is given by $I_0 = \int_0^L \left[(\partial_x Y)^2 + (\partial_x Z)^2 \right] dx$. In Eq. (1), F_e is the applied electrostatic force on the nanowire in the $-z$ direction due to an externally applied electric potential between the nanowire and the substrate. The potential has a dc component V_{dc} and an ac component V_{ac} with adjustable frequency f. The terms F_f^Y and F_f^Z in Eq. (1) represent the viscous damping forces in the y and z directions, respectively, which are modeled to be proportional to the velocity of the wire. Explicitly, the electrical force is given by[14]

$$F_e = -\frac{\pi \epsilon_0 V^2(t)}{(Z+h) \left[\ln \left(4 \frac{Z+h}{d} \right) \right]^2}, \quad (2)$$

and the viscous damping forces are

$$F_f^{\{Y,Z\}} = -\frac{\pi P d}{4 v_T} \partial_t \{Y, Z\}, \quad (3)$$

where h is the vertical distance between the clamped ends of the nanowire and the surface of the substrate, $d = 2r$ is the cross-sectional diameter of the wire, P is the air pressure, and $v_T = \sqrt{k_B T/m}$ is the air molecule velocity at temperature T. The expression of F_e is valid under the condition $h \gg d$. In this regime, the oscillation amplitude is about one order of magnitude smaller than that for the onset of the pull-in effect[16,17]. Also note that, the electrostatic force is *a priori* conservative and, thus, it would not lead to any net loss during a driving cycle. In general, the Ohmic loss associated with electrical force can be modeled[18] by a term proportional to the time derivative of $Z(x,t)$, as in a typical mechanical system. While this "electrical" source of dissipation can be included in a more accurate model of the driven nanowire system, the dominant source of dissipation in our study is fluid (viscous) damping. The Ohmic loss will become comparable in magnitude to viscous damping when the size of the nanowire is significantly reduced, say by at least one order of magnitude below the regime of our present study of multistability. For this reason the "electrical" dissipation term is neglected in the present work.

It has been known that surface effects[19–21] can become significant for nanosystems due to the reduction in the surface-to-volume ratio. However, such effects can still be modeled using the continuum model[19], and are negligible when the local-bending curvature is small. For example, tensile or compressive stress can be implemented in Eq. (1) by modifying the stretching elastic nonlinear terms in the Z and Y directions as $-Z_{xx}[SA + EA/(2L)2LI_0]$ and $-Y_{xx}[SA + EA/(2L)I_0]$, respectively, where S is the residual tensile or compressive stress. The tensile force can harden the beam and enhance the linear resonant frequency. This effect can shift the onset of non-planar motion[22] of the nanowire and affect the onset of chaotic motion[14]. Another issue concerns the geometrical shape of the nanowire. In experiments or nanodevice fabrication processes, a rectangular cross-sectional shape may be favored over a circular one. Such an alteration will affect the moment of inertia of the nanowire as well as the viscous damping coefficient. However, this will not lead to qualitatively different dynamical behaviors.

To solve Eq. (1), we begin with the standard FEM method[15] to derive element equations using a weighted residue formulation. We then assemble element equations to obtain a global matrix representation of the PDE system. After the FEM formulation, Eq. (1) is reduced to an initial value problem (IVP), which can be solved using the standard numerical integration methods. Specifically, we use the Runge-Kutta 4th-order Dormand-Prince pair embedded method[23] with adaptive step size control. Details of our method can be found in Appendix.
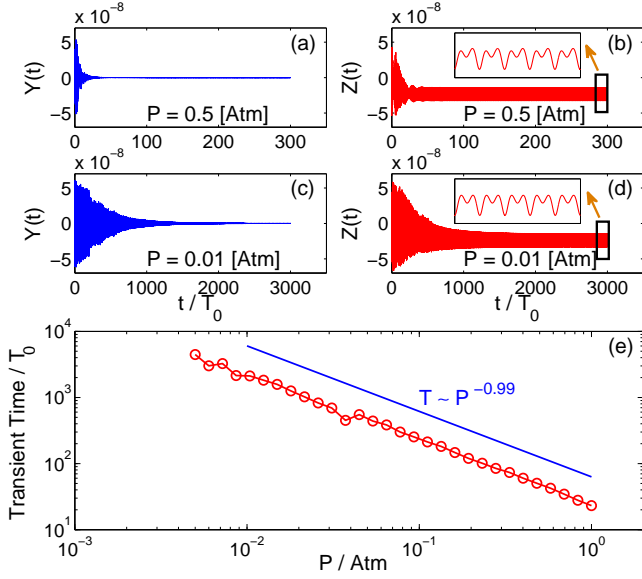
FIG. 2: (Color online) (a,b) For $P = 0.5$ atm, oscillations in the y (blue, left) and z (red, right) directions, respectively, of the center point of the nanowire, (c,d) similar plots but for $P = 0.01$ atm. The wire typically exhibits transient chaotic behavior before settling into a final state. For (a-d), the driving frequency is $f = f_0$. (e) Average transient time as a function of pressure. The threshold used for calculating the transient time is 1%. Note that all Y and Z values are represented in meters, if not specifically mentioned otherwise.

III. TRANSIENT DYNAMICS AND EMERGENCE OF MULTISTABILITY

The driven nanowire typically exhibits transiently chaotic motion before settling into a final steady state, which can be seen from Figs. 2(a-d), oscillations of the central point of the nanowire in the z and y directions for two values of the environmental pressure. Figure 2(e) shows the average transient time as a function of the pressure P. For each fixed value of P, the average time is obtained by using a number of initial configurations of the wire and calculating the time that the wire reaches the final state to within 1% for the first time. We observe that the average time scales with the pressure as a power law, with the exponent being approximately -1.

Insights into the inverse scaling law of the average transient time can be gained by considering a simple mechanical oscillator: $\ddot{x} + 2\beta\omega_0\dot{x} + \omega_0^2 x = 0$, where ω_0 is the angular frequency and β is the damping ratio. The amplitude solution follows an exponential decay form: $\exp(-t/\tau)$, where τ is the characteristic time. For damped oscillations, we have $\tau \sim 1/\beta$. Since pressure P is directly proportional to the damping ratio, we have $\tau \sim 1/P$. Similar effect can occur through variations in the temperature, as the quantity $1/\sqrt{T}$ plays a similar role as P in the dynamical evolution of the nanosystem.

In general, the role of damping due to collision with air molecules is important to the final vibration mode of the driven nanowire system. We find that, at low pressure (in contrast to ultrahigh vacuum), due to multistability and complex
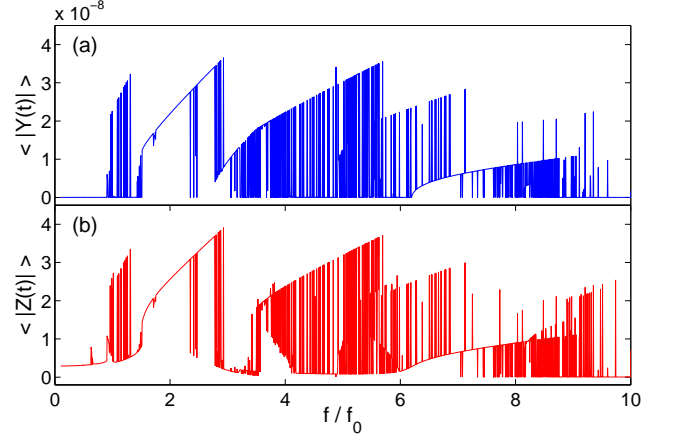

FIG. 3: (Color online) Frequency response of nanowire at pressure $P = 0.01$ atm. The motion of the center of the nanowire is monitored and the time-averaged amplitudes after the system reaches a steady state are computed. The average amplitudes in the y and z directions versus the driving frequency are shown in (a) and (b), respectively. The initial conditions are sinusoidal spatial functions with zero velocities in both y and z directions, and are fixed for all simulations at different frequencies. The parameter setting is: $E = 169$ GPa, $\rho = 2332$ kg/m^3, $V_{dc} = 5$V, $V_{ac} = 1$V, $L = 3$ μm, $d = 20$ nm, and $h = 0.2$ μm.

basin dynamics, the vibration amplitude can show an extreme sensitive dependence on the driving frequency of the external electrical force. At room conditions (~ 300 K, 1 atm), such a sensitive dependence is replaced by extensively chaotic motion of the nanowire[14]. In particular, the nanowire can exhibit a cascade of period-doubling bifurcations to relatively small-size chaotic attractors as a parameter, e.g., the magnitude of the ac component of the driving force, is increased. When the parameter exceeds a critical value, the small chaotic attractors can merge to generate extensive chaos, which has been suggested for potential applications such as extremely high frequency pseudo-random number generators[14]. Since the aim of the present work is complex dynamics associated with multistability, we focus on the low-pressure regime.

To demonstrate multistability, we investigate the frequency response of the nanowire system. The natural oscillation frequency of the nanowire can be estimated by using its mechanical and geometrical properties: $f_0 = 3.56\sqrt{EI/(\rho AL^4)}$. This formula gives $f_0 = 16.84$ MHz for the typical set of parameters indicated in Fig. 3. However, this estimated value f_0 is only to within an order-of-magnitude accuracy and therefore should not be taken as the true intrinsic frequency. The pressure is set to be 10^{-2} atm, which is much lower than that under room conditions but still far above that associated with ultrahigh vacuum condition, facilitating experimental study of the nanowire dynamics. Figure 3 shows simulation results for both in- and out-of-plane frequency responses, where extreme amplitude fluctuations are observed, implying multistability. In fact, a frequency analysis reveals *wide parameter regions in which multistability can arise*, as we now describe.

To carry out a frequency analysis to uncover the dynami-

cal mechanism for multistability in the driven nanowire system, we calculate the frequency response of the wire at typical low-pressure ($P = 0.01$ atm) and normal pressure ($P = 1$ atm) values, as shown in Figs. 3 and 4, respectively. Both figures show the average amplitudes as a function of the normalized frequency f/f_0 in the y, z directions after a transient time. Here, the normalized frequency is defined as $f_0 = 3.56\sqrt{EI/(\rho AL^4)}$, and the average is carried out in a large time interval. In Fig. 3, both y and z amplitudes exhibit an extreme type of fluctuations as the frequency is changed, indicating that an arbitrarily small change in the frequency can lead to a characteristically different final state. This provides strong evidence for multistability. (Further support for the coexistence of multiple states can be obtained by examining the phase diagram, as we will discuss below.) Compared with the case of low pressure (Fig. 3), the frequency responses under normal pressure are considerably smooth due to the relatively strong dissipation caused by collision with air molecules, as shown in Fig. 4. Apparently, for most frequency values, there is only one state remained after the transient phase. We note that, in Fig. 4(a), the peak about $f/f_0 = 3$, marked by the golden arrow, is the frequency that a previous work[14] used to identify the transition between planar and non-planar motions in the y direction (not the driving direction). This means that this peak can be turned on and off just by increasing or decreasing the ac component of the driving force. One cannot expect the same behavior to occur with the first peak (at $f/f_0 \approx 2$) or the third peak (at $f/f_0 \approx 6.3$), because they correspond to resonances associated with y and z motions and the magnitude of the external force will simultaneously affect the y and z responses. As a result, the oscillation mode will consistently be non-planar near these frequency values. On the contrary, the second peak in y does not correspond to a resonance in the z motion [Fig. 4(b)]. In fact, the amplitude in the z direction is always finite (not affected by the driving magnitude significantly), while the amplitude in the y direction can be switched on and off. A comparison between the low pressure and the normal pressure frequency responses suggests that all resonances in the normal pressure case are actually present in exactly the same position as in the low pressure case. One can thus think of the high pressure case as a derived state from the low-pressure regime by continuously increasing the pressure, and this can be explained by the fact that dissipation tends to destroy higher-frequency oscillations. An immediate conclusion is that, in a low-pressure environment, the driven nanowire system can exhibit high-dimensional transient chaos, associated with which multistable states occur typically.

To provide stronger support for the existence of multistability in the driven nanowire system, we use the method of *continuous frequency scan* in which a simulation starts from an initial frequency value and continues while incremental changes to the frequency are applied adiabatically in the sense that the frequency changes only when a steady state is reached. Insofar as there is a finite volume in the phase space surrounding the steady state (attractor), the trajectory tends to remain in the vicinity of the attractor when the frequency is changed adiabatically. The wild fluctuation patterns ob-
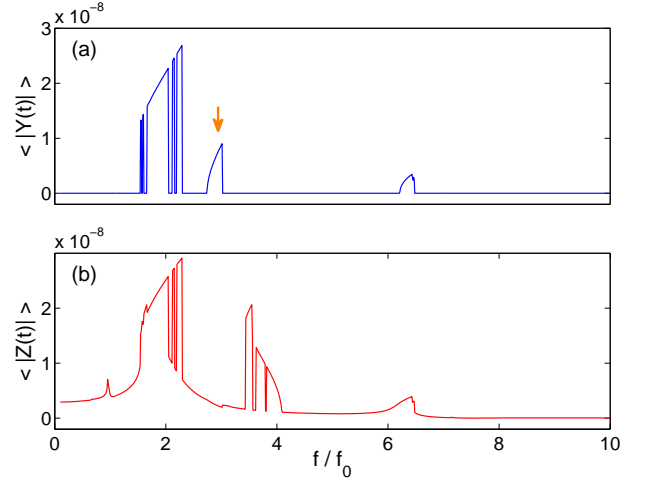

FIG. 4: (Color online) Frequency response of nanowire at pressure $P = 1$ atm. Other parameters are the same as Fig. 3.

served in Figs. 3(a) and 3(b) should then disappear. Nonetheless, some small peaks and valleys in the frequency response can still remain, due to the extreme instability at such locations. In our simulation, we start from the static sinusoidal initial condition in both y and z directions, and then keep increasing the frequency from $0.1f_0$ to $10f_0$ (forward scan, blue dashed lines in both panels of Fig. 5). When the frequency reaches the maximum value $10f_0$, we reverse the direction of the scan process (backward scan) by decreasing the frequency until it returns to $0.1f_0$ (indicated by red lines). Two more shorter forward scans are also performed starting from around $f/f_0 \approx 3.5$ to $f/f_0 \approx 6$ (as shown by black and cyan lines in both panels), but with different frequency resolutions. At $f/f_0 \approx 4.14$, we observe a fourfold stable region as depicted in the inset of Fig. 5(b). It is apparent from these results that stable attractors coexist in a wide parameter regime.

Emergence of multistability in the driven nanowire system can then be explained, as follows. To gain insights, we note that, for a common class of electrically driven microelectromechanical systems, a previous work based on a detailed bifurcation analysis of a reduced ODE model revealed that bistability can also be quite common[24]. In such a case, the two coexisting states are typically associated with high and low energy, respectively. Our driven nanowire system is an infinite dimensional dynamical system. In this system, the characteristic frequency response associated with bistability is a mirrored hysteresis-like peak, where forward and backward scan lead to relatively high- and low-energy states, respectively. Figure 6 shows the phase-space diagrams associated with the Z variable (Z versus v_z) for different frequencies. The panels (a,g,h), for example, show period 3, period 2, and period 3 behaviors, respectively, corresponding to the three small peaks around frequency $f/f_0 \approx 1$. Label (b) marks the small valley present in all frequency response diagrams at the start of the first resonance. Some phase diagrams indicate chaotic motions. The central panel compares responses from
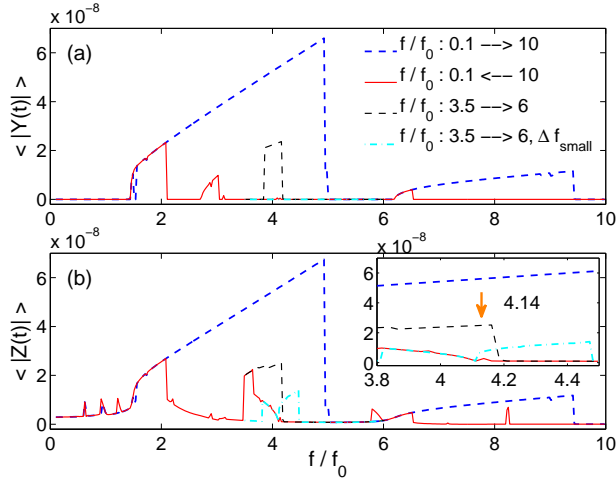
FIG. 5: (Color online) Continuous scan of frequency response of nanowire at low pressure $P = 0.01$ atm, where the frequency is adiabatically increased or decreased during the simulation and, for each fixed frequency, the average amplitudes associated with a steady state are calculated. Panels (a) and (b) show responses in the y, z directions, respectively. In both panels, blue (thick dashed) lines represent forward frequency scan from 0.1 to 10, red (solid) lines correspond to backward scan where the frequency is reduced adiabatically from 10 to 0.1, and black (thin dashed) and cyan (dash-dotted) lines both stand for forward scan from about 3.6 to 6, but a smaller frequency step size is used for the cyan (dash-dotted) lines. The inset of (b) is the zoom-in view of frequency around 4.14, where fourfold stability is observed.

FIG. 6: (Color online) Phase diagrams (z versus v_z) for different frequencies. The central panel compares results from the forward and backward scans to the separated frequency response of the nanowire. Multiple mirrored, hysteresis-like bistable regions are observed. Phase-space diagrams for z are plotted at locations labeled by letters, as shown in the upper and bottom rows.

the forward and backward continuous scans to the separated frequency response of the nanowire. We observe multiple, mirrored, hysteresis-like peaks at different resonant frequencies. The key feature is the overlap among the bistable frequency responses, which naturally leads to multistability. For example, the fourfold stable region in the inset of Fig. 5 is formed by the overlap of the two largest bistable regions in Fig. 6. The two states with largest amplitudes correspond to the mode similar to Fig. 6(c), and the other two correspond to Fig. 6(d) and 6(e), respectively. From these diagrams and their frequency values, we can conclude that, whenever there is a peak or valley emerging in the frequency response function, the system is at the boundary separating different basins of attraction where the system behavior is extremely difficult to be predicted. There are multiple directions or basins that the system can evolve into, and the typical phenomenon when the system is undergoing such change, as indicated by the phase diagrams, is period increasing, and quite frequently, chaotic motion will emerge. This is in fact transient chaos on the boundaries of the different basins.

IV. BASIN STRUCTURE AND CHARACTERIZATION

A natural question in the presence of multistability concerns the basin structure, because each coexisting stable state
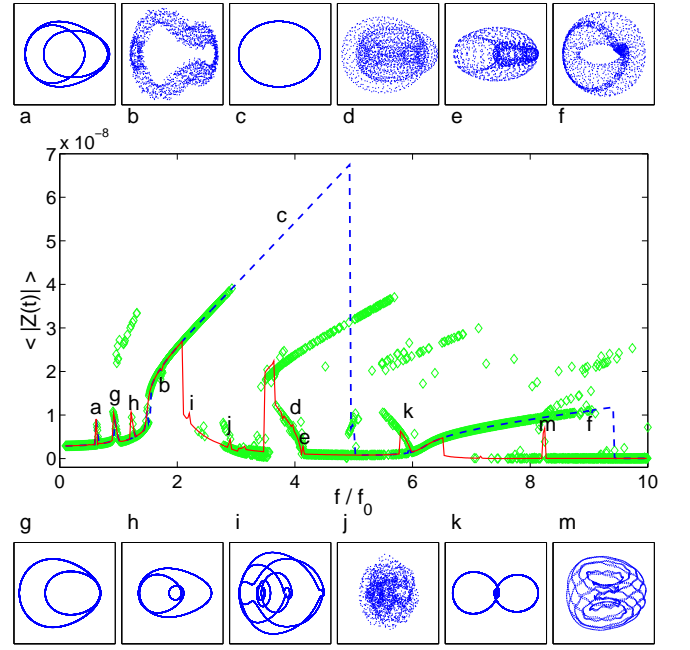
or attractor has its own basin of attraction. For the electrically driven nanowire system Eq. (1), a set of two coupled nonlinear PDEs, a difficulty is that the phase-space dimension of the system is infinite. In order to compute and visualize the basin structure, a two-dimensional representation of the phase space is desirable. While there are an uncountably infinite number of initial configurations for the entire wire, we can limit the choices of the initial configurations to those with spatially sinusoidal shape. For example, the initial z profile $Z(t = 0, x)$ and its velocity $V_z(t = 0, x)$ can be chosen as

$$Z(t = 0, x) = z_0 \sin(\pi x/L), \quad V_z(t = 0, x) = v_{z0} \sin(\pi x/L)$$
$$(4)$$

for $x \in [0, L]$. Fixing $Z(t = 0, x)$ and $V_z(t = 0, x)$ as in Eq. (4) and further fixing $V_y(t = 0, x) = 0$, we see that (z_0, v_{z0}) defines a two-dimensional "initial-condition" plane. Each point in the (z_0, v_{z0}) plane thus corresponds to a particular initial configuration of the wire, and we can compute to which attractor it leads to.

We choose the frequency to be $f/f_0 = 4.14$, where a fourfold stability region is observed. The initial configurations are randomly chosen within the rectangular two-dimensional representation of the phase-space region defined by $z_0 \in [-0.6h, 0.6h]$ and $v_{z0} \in [-60, 60]$m/s for the central point of the nanowire. The basin structure is plotted in Fig. 7(a), where different colors indicate the average amplitudes associated with different final attractors. In panels (b,c,d), the selected phase-space regions are successively magnified up to
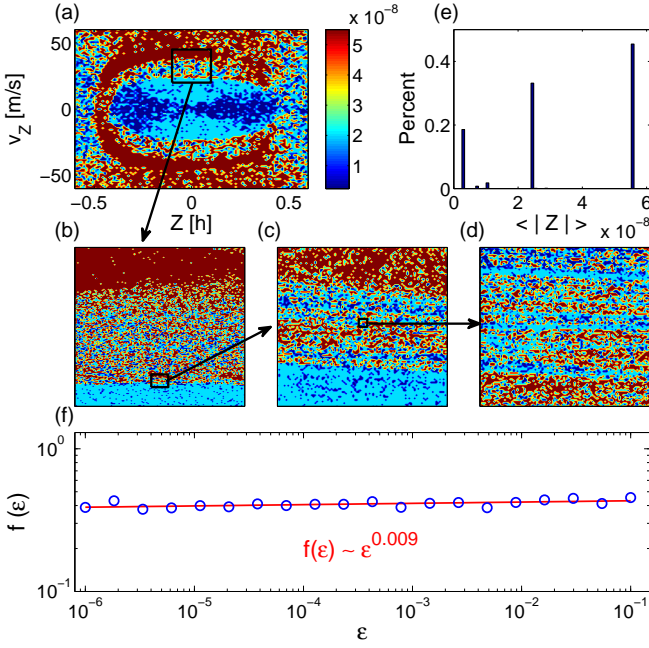
FIG. 7: (Color online) For initial configuration chosen according to $Z(t=0,x) = z_0 \sin(\pi x/L)$ and $V_z(t=0,x) = v_{z0} \sin(\pi x/L)$ ($x \in [0,L]$) and normalized frequency $f/f_0 = 4.14$, representative basin structures and successive magnifications, where the basins of different attractors are distinguished by different colors/gray-levels in (a-d). Panel (e) is a histogram of the amplitude associated with possible final states, where there are three large peaks, indicating at least three coexisting attractors. Panel (f) shows the algebraic scaling of the probability of error in the prediction of the final attractor, $f(\varepsilon)$, with ε, the error in the specification of the initial condition. The scaling exponent is $\alpha \approx 0.009$.

10^3 times, where qualitatively similar structures are observed. The coexisting attractors can also be implied from Fig. 7(e), a histogram of the amplitude associated with the possible final state. In particular, for each initial condition, we let the system evolve, record the time-averaged amplitude associated with the final oscillatory motion, and construct a histogram of the values of the time-averaged amplitude. We observe three large peaks in the histogram, indicating that most initial conditions lead to trajectories approaching asymptotically to these attractors.

The intermingled basin structure that appears to be invariant when successively smaller phase-space regions are examined indicates the difficulty to predict the final attractor from initial conditions having finite precision, because there are regions with the property that, for any initial condition that goes to one attractor, there are initial conditions arbitrarily nearby which lead to different attractors. The degree of unpredictability can be quantified by calculating the probability that a pair of slightly different initial conditions lead to distinct attractors. In particular, let ε be a small difference in the initial-condition pair and $f(\varepsilon)$ be this probability. As ε is decreased, we expect $f(\varepsilon)$ to decrease and, in general, we have $f(\varepsilon) \sim \varepsilon^\alpha$, where $0 \leq \alpha \leq 1$ is the so-called uncertainty exponent[25]. A repre-

sentative example of the scaling behavior of $f(\varepsilon)$ is shown in Fig. 7(f), where we obtain $\alpha \approx 0.009$. The near-zero value of the uncertainty exponent indicates an extreme degree of difficulty to predict the final attractor. For example, if ε is reduced by a factor of one million (which means that the precision in the specification of the initial condition is increased by six orders of magnitude), the probability of prediction error is reduced only by a factor of $(10^6)^{0.009} \approx 1.1$ - hardly any change. Such severe degree of unpredictability of the final state can also occur in low-dimensional chaotic systems, typically those with some kind of symmetry[1].

The near-zero value of the uncertainty exponent implies *extensive transient chaos* in the system. To argue for this, we recall the phenomenon of fractal basin boundaries in low-dimensional dynamical systems[25]. For a system whose phase-space dimension is N, if the basin boundary is smooth, then its dimension is $N-1$ (e.g., a smooth boundary in a two-dimensional phase space is a one-dimensional curve). For fractal basin boundaries, the dimension typically assumes a value between $N-1$ and N. There is mathematical proof[26] that in smooth dynamical systems, the dimension D_B of the fractal basin boundary is related to the uncertainty exponent as: $D_B = N-\alpha$. For $\alpha \approx 0$, we have $D_B \approx N$, which means that the fractal boundaries permeate the entire phase space. Dynamically, it has been established that fractal basin boundaries are due to transient chaos on the boundaries[25]. That the boundaries permeate the phase space stipulates that transient chaotic behavior also occurs in the entire phase space. It is in this sense which we say that transient chaos is extensive. In our nanowire system, the phase-space dimension is infinite, but the emergence of multistability and basin boundaries with near-zero uncertainty exponent can still be taken as strong indication that the underlying transient chaotic behavior is extensive.

A physically important issue concerns the effect of noise. For a nanowire system in a realistic operating environment (e.g., modest pressure and room temperature), the dominant noise sources are thermal fluctuations and pressure instability. As for low-dimensional systems, we find that noise can induce switching among the multiple coexisting states. In fact, similar behaviors were observed in another nanoscale, high-dimensional system: the semiconductor superlattice[6,7].

V. UBIQUITY OF MULTISTABILITY IN DRIVEN NANOWIRE SYSTEM

We have demonstrated the emergence of the multistable states in the driven nanowire system, and the underlying dynamical mechanism. A question is how ubiquitous multistability is in nanosystems. Here we address this question by considering variations in several parameters, with the result that multistability can be expected to occur commonly in nanoscale systems.

We first consider the effect of varying dc voltage. As shown in Fig. 8, varying dc voltage can shift the unstable frequency regions. Moreover, a larger dc voltage can lead to stronger fluctuations at high frequency, due to the increase in
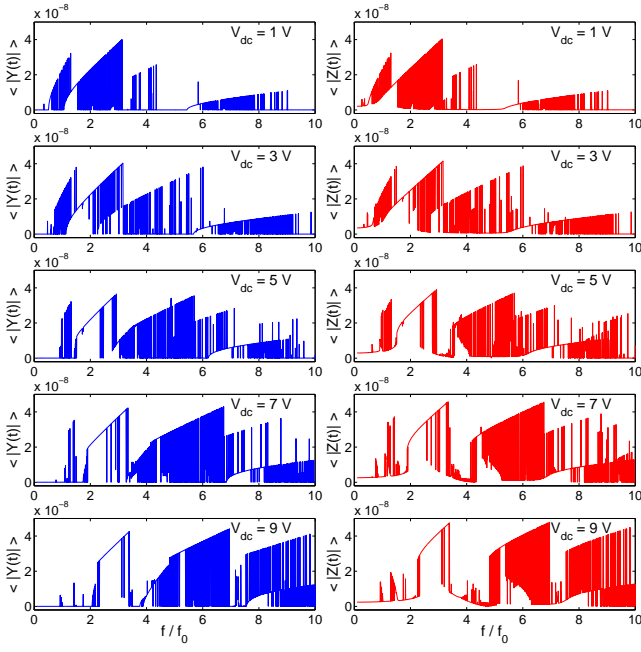
FIG. 8: (Color online) Comparison of frequency responses for the same system with different dc voltages (V_{dc}). The left and right columns represent the frequency responses in the y and z directions, respectively. From top to bottom row, the dc values are $1, 3, 5, 7, 9$ V, in order. All simulations are performed using parameters: $V_{ac} = 1$ V, $P = 0.01$ atm, $T = 300$ K, $L = 3$ μm, $h = 0.2$ μm, $d = 20$ nm.
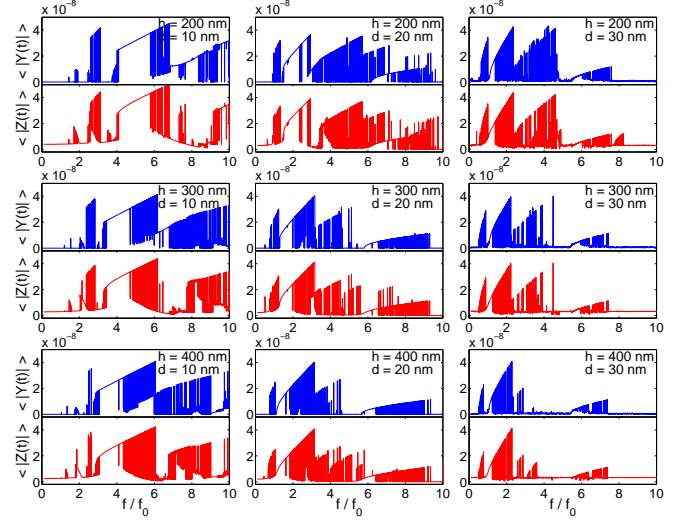

FIG. 9: (Color online) Effect of gate trench height h and the nanowire diameter d on the frequency response. From top to bottom row, $h = 200, 300, 400$ nm, respectively. From left to right column, $d = 10, 20, 30$ nm, respectively. Other parameters are $V_{dc} = 5$ V, $V_{ac} = 1$ V, $P = 0.01$ atm, $T = 300$ K, wire length $L = 3$ μm.
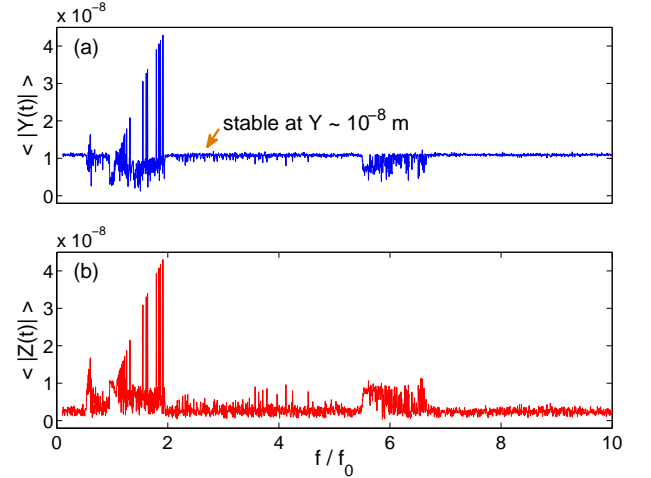

FIG. 10: (Color online) Extreme case of hardening wire frequency response. Except $h = 400$ nm, and $d = 40$ nm, other parameters are the same as in Fig. 9.

the total driving energy input. For example, for $V_{dc} = 1$, most unstable/frequency sensitive states can be found in the low-frequency regime, but small amplitude fluctuations occur in the high-frequency regime. As V_{dc} is increased, higher-frequency states with larger amplitudes emerge and, at the same time, low-frequency region becomes more stable, typically settling into one of the original states. This results in a shift of the highly unstable regions towards higher frequency values. This shifting behavior can be tracked by the movement of the signature features indicated by golden arrows in Fig. 8. Also, the peaks become sharper on edges for increased dc values.

Besides ac and dc voltages, it is also of interest, especially from the point of view of experimental study, to vary the system-design parameters such as the dimension of the nanowire or the gate. Here, we present results of changing two of these key parameters, the gate trench height h and the diameter of the nanowire d. The two parameters both appear in the formulation of the driving force, and thus should be considered concurrently. Because our formulation of the driving force is based on the capacitance expression of the capacitor from the nanowire segment in conjunction with the gate electrodes, a valid force expression requires $h \gg d$. Taking these into consideration, we study the oscillations of the system for a series of combinations of (h, d) pairs, as shown in Fig. 9. We see that, an increase in either h or d can stabilize the system. However, a larger value of h tends to stabilize the oscillation

in different frequency regions uniformly, whereas a thicker wire (larger values of d) tends suppress high-frequency oscillations. Figure 10 shows an extreme example of the beam hardening behavior, where most multistable states, especially those with large amplitudes, disappear. Another interesting behavior for is that, due to the hardening effect, in the Y direction, the beam stabilizes at about 10nm instead of zero vibration amplitude as in other cases. In addition, multiple states of smaller amplitudes are present in the Y oscillations.

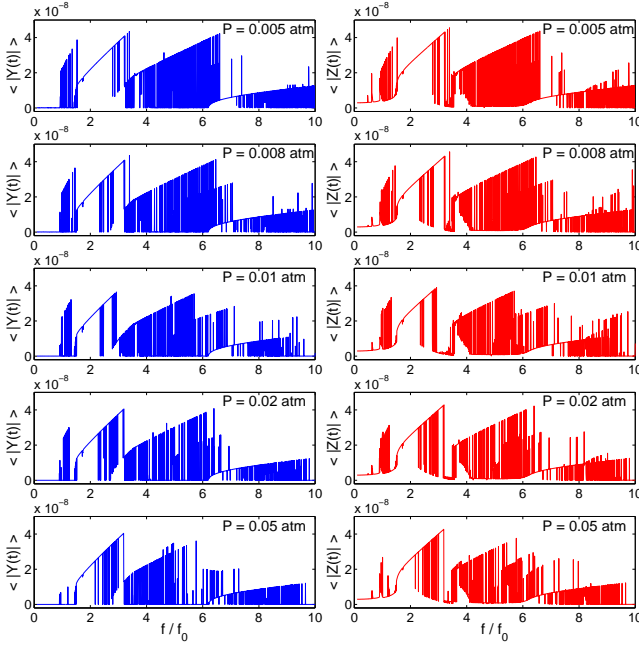Finally, we discuss the effect of varying environmental pressure. As mentioned, the normal pressure ($P = 1$ atm)

FIG. 11: (Color online) Comparison of frequency responses for the same system with slightly changing pressure (P). The left and right columns represent the frequency responses in the y and z directions, respectively. From top to bottom row, the pressure values are $0.005, 0.008, 0.01, 0.02, 0.05$ atm, in order. All simulations are performed using parameters: $V_{dc} = 5$ V, $V_{ac} = 1$ V, $T = 300$ K, $L = 3$ μm, $h = 0.2$ μm, $d = 20$ nm.

regime can be regarded as an extension from the low pressure regime, where the final stable state is a continuation of one of the multiple stable states under low pressure. From Fig. 11 we can see how high frequency oscillations are gradually destroyed as the pressure is increased. An implication of potential application from such "survival" process would be to use pressure as a control parameter to select the relative proportion of the multistable states.

VI. CONCLUSION

To summarize, we focus on the working regime in between room conditions and ultrahigh vacuum. This regime can be realized relatively readily in experimental studies, in which we find a number of interesting dynamical phenomena such as multistability, complex basin structures - leading to a fundamental difficulty in terms of prediction of the final state, and extensive transient chaos as the dynamical origin of the complex basin structure. To our knowledge, this is the first comprehensive study of multistability in high-dimensional, nanoscale physical systems.

A possible experimental scheme to test the findings of this paper is as follows. Due to the extensive nature of transient chaos leading to basin boundaries permeating the phase space, random perturbations can cause the system to "hop" from one attractor to another in an intermittent manner. Experimentally one can add a stochastic voltage signal to the sinusoidal driving and monitor the motion of the nanowire. The occurrence of intermittency, i.e., the system's exhibiting one type of periodic motion for a finite duration of time and then switching to another, is indication of multistability. Persistence of the intermittent behavior regardless of how the amplitude of the stochastic voltage signal changes implies complex basin structure and extensive transient chaos.

Appendix: Efficient finite-element method for electrostatically driven Si-nanowire

The physically detailed model of electrostatically driven Si-nanowire is a set of nonlinear PDEs with integrals of the dynamical variables. While the system can be solved using the standard finite-element method (FEM), where the partial derivatives, the integrals, and the nonlinear forces are evaluated completely numerically, the computations turn out to be extremely intensive, prohibiting systematic and comprehensive analysis of the model. We realize that many quantities associated with the FEM for this class of systems can in fact be evaluated analytically, which can help reduce the computation significantly. Motivated by this, we have developed an improved FEM, which entails an efficient procedure that combines analytic evaluation, numerical discretization and integration to solve the nonlinear PDE system. Below is a description of the mathematical formulation of our method.

Finite-element formulation. To formulate a finite-element (FE) solution, we rewrite Eq. (1) in the following compact form:

$$-\ddot{Y} + c_1\dot{Y} + c_2 Y'''' + c_3 I_0 Y'' = 0,$$
$$-\ddot{Z} + c_1\dot{Z} + c_2 Z'''' + c_3 I_0 Z'' + F_e = 0, \tag{5}$$

where primes and dots represent derivatives with respect to x and t, respectively, the coefficients are

$$c_1 = -\frac{\pi P d}{4\rho A v_T}, \qquad c_2 = -\frac{EI}{\rho A}, \qquad c_3 = \frac{E}{2\rho L}, \tag{6}$$

and the electrical force F_e has been normalized by the factor $1/(\rho A)$. The basic steps in a typical FE formulation are: discretization, choosing approximation model and basis functions, deriving element equations using the weighted residue method, assembling element equations to get the global matrix representation of the problem, and solving a set of initial value problems (ODE set).

Discretization. First we divide the x-axis equally into N element ranges, with the element index e running from 1 to N, as shown in Fig. 12. For each element e, we have $x \in [x_{e-1}, x_e]$ and $x_e - x_{e-1} = \ell = L/N$. Because the two ends of the wire are clamped, we have $\{Y, Z\}(\{0, L\}, t) = 0$, and $\{Y', Z'\}(\{0, L\}, t) = 0$, which are the boundary conditions for generating a unique solution.

Basis functions. To preserve the physical condition of continuity of beam deflections, the nodal displacement values must be matched between the neighboring elements. To obtain physically correct results that require smoothness, a second-order approximation can be used so that both the displacement and the slope of the wire at the nodal points are continuous between neighboring elements. Consequently, for element e, at least second-order or four degrees-of-freedom, i.e., $Z(x_{e-1}), Z'(x_{e-1}), Z(x_e), Z'(x_e)$, at both ends of the element, are needed. In this setup, each node has two unknown values, and there are $2(N-1)$ unknowns in total for the whole nanowire (excluding the two clamped ends).

Having obtained the nodal values of element e, we can use the interpolation approximation model, for example, to express $Z(x, t)$ as

$$Z^e(x, t) = \sum_{i=1}^{4} \phi_i(x) q_i^e(t) = \phi^T q^e, \quad (7)$$

where $\phi_i(x)$ are the basis functions to be computed, and $q^e(t) = [Z(x_{e-1}, t), Z'(x_{e-1}, t), Z(x_e, t), Z'(x_e, t)]^T$ is the unknown vector for element e. To compute a general set of basis functions, we let $\bar{x} = x - x_{e-1}, \bar{x} \in [0, \ell]$, and $s = \bar{x}/\ell$, $s \in [0, 1]$. Assuming that each element has four degrees-of-freedom, we can express the displacement in terms of a third-order polynomial, as follows:

$$Z^e(\bar{x}) = \begin{bmatrix} 1 & \bar{x} & \bar{x}^2 & \bar{x}^3 \end{bmatrix} \begin{bmatrix} a_0^e & a_1^e & a_2^e & a_3^e \end{bmatrix}^T = XA^e,$$

so $Z^{e\prime}(\bar{x}) = X'A^e$. Using the expression for $Z^e(\bar{x})$ and $Z^{e\prime}(\bar{x})$, and setting $\bar{x} = 0, \ell$, we obtain the following expression of q^e in terms of A^e:

$$q^e = \begin{bmatrix} 1 & 0 & 0 & 0 \\ 0 & 1 & 0 & 0 \\ 1 & \ell & \ell^2 & \ell^3 \\ 0 & 1 & 2\ell & 3\ell^2 \end{bmatrix} A^e = BA^e.$$

The displacement $Z^e(\bar{x})$ can then be written as

$$Z^e(\bar{x}) = XA^e = XB^{-1}q^e. \quad (8)$$

Comparing Eqs. (8) with (7), we find that the basis functions in terms of s are $\phi = XB^{-1} = [1 - 3s^2 + 2s^3, \ell s(1 - 2s + s^2), s^2(3 - 2s), \ell s^2(s - 1)]^T$.

Element equations. We use a standard weighted-residue method in finite-element analysis to derive the element equations, where the selection of weight functions is key. We use Galerkin's formulation[15], where the basis functions are selected as the weight functions. The method requires, for element e, the following:

$$\int_{x_{e-1}}^{x_e} \left(-\ddot{Z} + c_1\dot{Z} + c_2 Z'''' + c_3 I_0 Z'' + F_e \right) \phi_i(x) dx = 0, \quad (9)$$
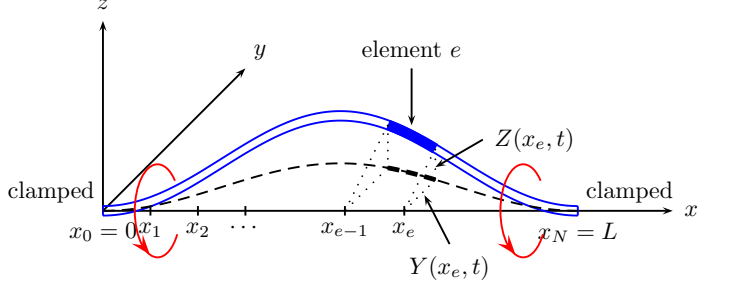
for $i = 1, 2, 3, 4$. Integrating by parts, we have

$$\int_{x_{e-1}}^{x_e} \ddot{Z}\phi_i(x)dx = c_1 \int_{x_{e-1}}^{x_e} \dot{Z}\phi_i(x)dx + c_2 \int_{x_{e-1}}^{x_e} Z''\phi_i''(x)dx$$
$$+ c_1\left(Z'''\phi_i - Z''\phi_i' \right)\Big|_{x_{e-1}}^{x_e} + c_3 I_0 \int_{x_{e-1}}^{x_e} Z''\phi_i(x)dx \quad (10)$$
$$+ \int_{x_{e-1}}^{x_e} F_e\phi_i(x)dx.$$

Substituting Eq. (7) into the above equation, we reduce it to the following matrix representation:

$$M_1^e \ddot{q}^e = c_1 M_1^e \dot{q}^e + (c_2 M_2^e + c_3 I_0 M_3^e)q^e + f_{gen}^e + f_{ext}^e \quad (11)$$

where the elements of the matrices are given by

$$M_1^e(i, j) = \int_{x_{e-1}}^{x_e} \phi_i(x)\phi_j(x)dx,$$
$$M_2^e(i, j) = \int_{x_{e-1}}^{x_e} \phi_i''(x)\phi_j''(x)dx,$$
$$M_3^e(i, j) = \int_{x_{e-1}}^{x_e} \phi_i(x)\phi_j''(x)dx,$$
$$M_4(i, j) = \int_{x_{e-1}}^{x_e} \phi_i'(x)\phi_j'(x)dx.$$

Note that element M_4, which is used for calculating I_0, is listed here for completeness. While the integral range is element dependent, the basis functions are universal. The matrix elements can be found by using the normalized variable s for integration. The term $c_1\left(Z'''\phi_i - Z''\phi_i' \right)\Big|_{x_{e-1}}^{x_e}$ is the generalized force vector for the element, which can be expressed as

$$f_{gen}^e = [Q_1^e, P_1^e, Q_2^e, P_2^e]T,$$

where $Q_1^e = -Z'''(x_{e-1})$, $Q_2^e = Z'''(x_e)$, $P_1^e = -Z''(x_{e-1})$, $P_2^e = -Z''(x_e)$, and subscripts 1 and 2 are for the left and right nodes, respectively. These forces are also required to satisfy the inter-element continuity condition if no external forces, as in our case, are applied on the connecting

FIG. 12: Schematic picture of element division using Finite-Element Method.

nodes. In fact, the general forces of neighboring elements e and $e+1$ must satisfy

$$Q_2^e + Q_1^{e+1} = 0, \qquad e = 1, 2, \ldots, N-1, \qquad (12)$$

and so does P. These conditions can simplify the next step, namely, assembly, substantially.

The last term in Eq. (11) is the external force vector f_{ext}^e. The integral term on the external force $F_e(x, t)$ can be computed either by direct analytical integration or approximated method, depending on the exact form of the force and its behavior over the whole domain. If the integral cannot be evaluated analytically, we can use numerical integration in case the force has large deviation over a single element, or we can simply expand the force if it is a spatially slowly varying function. For our nanowire system, the electrostatic force F_e is in fact a slowly changing function with respect z, because of the condition $h \gg z$. Thus, we can use linear approximation of F_e

$$F_e(s, t) = (1-s)f_1(t) + sf_2(t), \qquad (13)$$

where f_1 and f_2 are the forces exerted on the two nodes of the element. *The great advantage is that the integrals in the external force vector can be analytically calculated since they are over polynomials, making the whole computational process extremely efficient.*

Assembly. Having obtained the 4×4 matrix representation of element equations, Eq. (11), we can assemble them in a proper way to derive the global equation of motion by using the fact that each node x_i ($i \neq 0, N$) is shared by two elements. In the matrix representation, adding the contributions from the two neighboring elements on one shared node is equivalent to shifting a direct sum of element matrices $M_i^{e'}s$ ($i = 1, 2, 3$), which can be expressed as

$$M_i^{All} = \left(\oplus_{k=1}^{\lceil \frac{N}{2} \rceil} M_i^e \right) \oplus \mathbf{0}_{1+(-1)^N} \qquad (14)$$
$$+ \mathbf{0}_2 \oplus \left(\oplus_{k=1}^{\lfloor \frac{N}{2} \rfloor} M_i^e \right) \oplus \mathbf{0}_{1-(-1)^N},$$

for $i = 1, 2, 3$, where M_i^{All} is a $2(N+1) \times 2(N+1)$ global assembled matrix for M_i^e, and $\mathbf{0}_j$ is a $j \times j$ zero matrix. This assembly equation means the following: letting 4×4 matrix M_i^e be the upper left block of the assembled matrix M_i^{All}, then increasing both row and column indices by 2, and adding M_i^e again. We then repeat this process until M_i^{All} reaches the desired dimension, $2(N+1) \times 2(N+1)$.

Next, we assemble the general and external force vectors into the corresponding global quantities by using the same technique. Using the continuity condition Eq. (12) and the approximation Eq. (13), we have, for the general and external

force vectors, the following:

$$f_{gen}^{All} = \begin{bmatrix} Q_0 \\ P_0 \\ 0 \\ \vdots \\ 0 \\ \hline Q_N \\ P_N \end{bmatrix} \quad \text{and} \qquad (15)$$

$$f_{ext}^{All} = \begin{bmatrix} \ell(7f_0 + 3f_1)/20 \\ \ell^2(3f_0 + 2f_1)/60 \\ \hline \ell(3f_0 + 14f_1 + 3f_2)/20 \\ \ell^2(-f_0 + f_2)/30 \\ \cdots \\ \ell(3f_{N-2} + 14f_{N-1} + 3f_N)/20 \\ \ell^2(-f_{N-2} + f_N)/30 \\ \hline \ell(3f_{N-1} + 7f_N)/20 \\ \ell^2(-2f_{N-1} - 3f_N)/60 \end{bmatrix},$$

where we have used global subscripts from 0 to N. Notice that the nodes 0 and N represent the two clamped ends of the wire, so their displacements and slopes are always zero. As mentioned earlier, we have only $2(N-1)$ unknowns defined as the assembled $q^e{}'s$

$$\mathbf{Z} = [Z_1, Z_1', Z_2, Z_2', \ldots, Z_{N-1}, Z_{N-1}']^T,$$

and $\mathbf{Y}$ can be defined in a similar way. The matrices M_i^{All} and the force vectors f_{gen}^{All}, f_{ext}^{All} should be modified accordingly. As shown in Eq. (15), the first and last two components of the vectors should be cut off so that

$$f_{gen} = 0, \qquad f_{ext}(i) = f_{ext}^{All}(i+2), \qquad 1 \le i \le 2(N-1).$$

The first and last two rows and columns should be cut off for M_i^{All},

$$M_k(i, j) = M_k^{All}(i+2, j+2)$$

for $k = 1, 2, 3$ and $1 \le i, j \le 2(N-1)$. After assembly and modification, we convert Eq. (11) into the following global matrix form of equations of motion:

$$\ddot{\mathbf{Y}} = c_1 \dot{\mathbf{Y}} + (c_2 M_1^{-1} M_2 + c_3 I_0 M_1^{-1} M_3)\mathbf{Y}, \qquad (16)$$
$$\ddot{\mathbf{Z}} = c_1 \dot{\mathbf{Z}} + (c_2 M_1^{-1} M_2 + c_3 I_0 M_1^{-1} M_3)\mathbf{Z} + M_1^{-1} f_{ext}.$$

Calculation of I_0. In Eq. (16), the only unknown coefficient is I_0, which is twice the change in the original length of the nanowire under nonlinear stretching. We can rewrite I_0 as $I_0 = I_0^Y + I_0^Z$, where

$$I_0^Z = \int_0^L (\partial_x Z)^2 dx.$$

To calculate this integral, we substitute the basis expansion of

$Z(x,t)$, Eq. (7), into I_0^Z, and obtain

$$
\begin{aligned}
I_0^Z &= \sum_{e=1}^{N} \int_{x_{e-1}}^{x_e} \sum_{i,j=1}^{4} \phi_i'(x)\phi_j'(x)q_i^e q_j^e dx \\
&= \sum_{i,j=1}^{4} \left(\int_{x_{e-1}}^{x_e} \phi_i'(x)\phi_j'(x)dx \right) \sum_{e=1}^{N} q_i^e q_j^e \\
&= \sum_{i,j=1}^{4} M_4(i,j) \sum_{e=1}^{N} q_i^e q_j^e.
\end{aligned}
$$

Similarly, using the expansion $Y^e(x,t) = \sum_{i=1}^{4} \phi_i(x)p_i^e(t)$, we can compute I_0^Y. Finally, we obtain

$$
I_0 = \sum_{i,j=1}^{4} M_4(i,j) \sum_{e=1}^{N} (q_i^e q_j^e + p_i^e p_j^e). \tag{17}
$$

Solving the initial value problem (IVP). Equation (16) represents an initial-value problem (IVP) which can be solved using the standard numerical integration methods. For example, in the absence of random fluctuations, we can use the Runge-Kutta 4th-order Dormand-Prince pair embedded method[23] with adaptive step size control to solve the following transformed first order ODE set:

$$
\frac{d}{dt}
\begin{bmatrix}
\boldsymbol{Y} \\
\boldsymbol{Y}^t \\
\boldsymbol{Z} \\
\boldsymbol{Z}^t
\end{bmatrix}
= \tag{18}
$$

$$
\begin{bmatrix}
\boldsymbol{Y}^t \\
c_1\boldsymbol{Y}^t + (c_2 M_1^{-1} M_2 + c_3 I_0 M_1^{-1} M_3)\boldsymbol{Y} \\
\boldsymbol{Z}^t \\
c_1\boldsymbol{Z}^t + (c_2 M_1^{-1} M_2 + c_3 I_0 M_1^{-1} M_3)\boldsymbol{Z} + M_1^{-1} f_{ext}
\end{bmatrix}
$$

with the initial condition

$$
\begin{bmatrix}
\boldsymbol{Y}(0) \\
\boldsymbol{Y}^t(0) \\
\boldsymbol{Z}(0) \\
\boldsymbol{Z}^t(0)
\end{bmatrix}
=
\begin{bmatrix}
\boldsymbol{Y}_0 \\
\boldsymbol{Y}_0^t \\
\boldsymbol{Z}_0 \\
\boldsymbol{Z}_0^t
\end{bmatrix}. \tag{19}
$$

In conventional MD simulations, due to the requirement of energy conservation, relatively simple, second-order implicit methods such as the Verlet leapfrog algorithm are usually used. However, more sophisticated, 4th-order method such as the traditional Gear algorithm[27] exists for integrating Hamiltonian systems. The improved 4th-order method developed by Martyna and Tuckerman[28] retains the basic properties of the Gear method but is both symplectic and time-reversible. Our driven nanowire system, however, is dissipative, so a symplectic reversible integrator is not necessary. We choose the standard 4th-order Runge-Kutta method due to its high stability and efficiency. When random fluctuations are present, Eq. (16) can be solved by the standard second-order method for solving stochastic ODEs[29].

[1] Y.-C. Lai and T. Tél, *Transient Chaos* (Springer, New York, 2011).

[2] U. Feudel and C. Grebogi, Chaos **7**, 597 (1997); U. Feudel and C. Grebogi, Phys. Rev. Lett. **91**, 134102 (2003).

[3] Y. T. Yang, C. Callegari, X. L. Feng, K. L. Ekinci, and M. L. Roukes, Nano Lett. **6**, 583 (2006).

[4] D. Rugar, R. Budakian, H. Mamin, and B. Chui, Nature **43**, 329 (2004).

[5] P. Gammel, G. Fischer, and J. Bouchaud, Bell Labs Technical J. **29** (2005).

[6] M. Patra, G. Schwarz, and E. Schöll, Phys. Rev. B **57**, 1824 (1998).

[7] Yu. Bomze, R. Hey, H. T. Grahn, and S. W. Teitsworth, Phys. Rev. Lett. **109**, 026801 (2012).

[8] See, for example, P. Kim and C. M. Lieber, Science **286**, 2148 (1999); T. Rueckes *et al.*, Science **289**, 94 (2000); M. Dequesnes, S. V. Rotkin, and N. R. Aluru, Nanotechnology **13**, 120 (2002); D. G. Hasko, J. E. Jung, and J. M. Kim, Appl. Phys. Lett. **86**, 083105 (2005); J. S. Aldridge and A. N. Cleland, Phys. Rev. Lett. **94**, 156403 (2005); E. Buks and B. Yurke, Phys. Rev. E **74**, 046619 (2006); I. Kozinsky *et al.*, Appl. Phys. Lett. **88**, 253101 (2006); S. N. Cha *et al.*, Nano Lett. **8**, 1590 (2008).

[9] I. Kozinsky, H. W. C. Postma, O. Kogan, A. Husain, and M. L. Roukes, Phys. Rev. Lett. **99**, 207201 (2007). This work treated multiple coexisting attractors and basins of attraction in a nano mechanical resonating system. The system was specifically designed so that it can be described by the classic Duffing's equation. In particular, the study was carried out in a vacuum environment at low temperatures and, a strong magnetic force was used to enable modeling of the system by a second-order ordinary differential equation under driving. In contrast, our nanowire system is driven electrically so that modeling based on nonlinear partial differential equation is absolutely necessary. Our system thus represents truly a very high-dimensional dynamical system in a more realistic setting (e.g., low but not near zero ambient pressure and room temperature) for which multistability and complicated basin structures had not been reported prior to our study.

[10] N. Kacem and S. Hentz, Appl. Phys. Lett. **95**, 183104 (2009).

[11] Y. Gerson, S. Krylov, B. Ilic, and D. Schreiber, Finite Elem. Anal. Des. **49**, 58-69 (2012).

[12] S. Shim, M. Imboden, and P. Mohanty, Science **316**, 95 (2007).

[13] D. N. Guerra, T. Dunn and P. Mohanty Nano Lett. **9**, 3096 (2009); T. Dunn, D. N. Guerra and P. Mohanty Eur. Phys. J. B **69**, 5 (2009).

[14] Q.-F. Chen, L. Huang, Y.-C. Lai, C. Grebogi, and D. Dietz, Nano Lett. **10**, 406 (2010).

[15] C. S. Desai and T. Kundu, *Introductory finite element method*

(CRC Press, Boca Raton, 2001); G. E. Karniadakis and S. Sherwin, *Spectral/hp element methods for computational fluid dynamics* (Oxford University Press, Oxford, UK, 2005); J. N. Reddy, *An Introduction to the Finite Element Method* (McGraw-Hill Publications, New York, 2006).

[16] M. Dequesnes, S. V. Rotkin, and N. R. Aluru, Nanotechnology **13**, 120 (2002).

[17] S. N. Cha, J. E. Jang, Y. Choi, G. A. J. Amaratunga, D. J. Kang, D. G. Hasko, J. E. Jung, and J. M. Kim, Appl. Phys. Lett. **86**, 083105 (2005).

[18] V. A. Sazonova, *A Tunable Carbon Nanotube Resonator*, PhD Dissertation Cornell University, Ithaca, New York (2006).

[19] J. B. Ma, L. Jiang, and S. F. Asokanthan, Nanotechnology **21**, 505708 (2010).

[20] Y. T. Yang, C. Callegari, X. L. Feng, and M. L. Roukes, Nano Letters **11**, 1753-1759 (2011).

[21] H. S. Park, J. Appl. Phys. **103** 123504 (2008).

[22] W. Conley, A. Raman, C. Krousgrill, and S. Mohammadi, Nano Lett. **8**, 1590 (2008).

[23] J. R. Dormand and P. J. Prince, J. Comput. Appl. Math. **6**, 1 (1980).

[24] Q.-F. Chen, L. Huang, and Y.-C. Lai, Chaos **18**, 013103 (2008).

[25] C. Grebogi, S. W. McDonald, E. Ott, and J. A. Yorke, Phys. Lett. A **99**, 415 (1983); S. W. McDonald, C. Grebogi, E. Ott, and J. A. Yorke, Physica D **17**, 125 (1985).

[26] C. Grebogi, H. E. Nusse, E. Ott, and J. A. Yorke, in *Dynamical Systems*, edited by J. C. Alexander, Lecture Notes in Math. **1342**, 220 (Springer-Verlag, Berlin, 1988).

[27] C. W. Gear, *Numerical Initial Value Problems in Ordinary Differential Equations* (Prentice-Hall, Englewood Cliffs, 1971).

[28] G. J. Martyna and M. E. Tuckerman, J. Chem. Phys. **102**, 8071 (1995).

[29] C. W. Gardiner, *Handbook of Stochastic Methods* (Springer, New York, 1985).